

Contact-free Magnetic Clutch Applied for Flywheel Cell System

Nan-Chyuan Tsai and Hong-Seng Aw

Department of Mechanical Engineering, National Cheng Kung University, 70101, Tainan City, Taiwan

Keywords: Servo Gap-Retained Mechanism, Hybrid Magnetic Actuator, Feedback-Linearized Sliding Mode Control.

Abstract: A TDOF (Two Degrees of Freedom) Servo Gap-Retained Mechanism (SGRM) is proposed and verified by experiments. It consists of a flywheel and an Intelligent Posture Tracking System (IPTS). The flywheel is regarded as the tracking objective of the IPTS. The IPTS is mainly composed by an intelligent disc and two pairs of Hybrid Magnetic Actuators (HMAs). The posture of the intelligent disc is controlled by the magnetic forces induced by the HMAs to retain a constant gap with respect to the eccentric flywheel. Since the HMA is highly nonlinear, a Feedback-Linearized Sliding Mode Control (FLSMC) is synthesized to account for system parameter nonlinearities. The proposed SGRM is part of the flywheel cell system. When the MGU (Motor/Generator Unit) in flywheel cell operates at idle mode, the shaft of flywheel will be separated from MGU in order to avoid the energy loss of the flywheel by the back EMF induced by the magnetic field of MGU. The shaft of flywheel and MGU still need to maintain synchronous power transmission so that a contact-free clutch has to be equipped. The role of SGRM in a flywheel cell is to ensure the centerline of the flywheel properly is aligned with the magnetic clutch. Intensive experimental simulations are undertaken to verify the feasibility of the proposed SGRM and FLSMC.

1 INTRODUCTION

Recently, due to the green and diverse types of energy gradually emphasized, Flywheel Energy Storage System (FESS) has become a popular choice because of its inherent properties of free pollution and fairly short rise time. In general, the flywheel cell is equipped with a Motor-Generator Unit (MGU) in a vacuum chamber. However, the kinetic energy loss due to the interaction (i.e., back EMF effect) between flywheel shaft and MGU is the most serious issue and has to be avoided. This problem can be solved by separating the MGU from the flywheel *via* a non-contact electromagnetic clutch which can transmit required torque, without physical contact, between MGU and flywheel. Most importantly, for high-efficient power transmission, the gap between the active rotor, connected to the MGU, and the counter-part, passively driven by the active rotor, at the electromagnetic clutch has to be retained as constant all the time (Li, 2009). In other words, the SGRM is the key to the electromagnetic clutch being able to align the shaft of flywheel with the centerline of MGU.

A SGRM with two pairs of Hybrid Magnetic

Actuators (HMAs) is proposed and verified by experiments. In order to achieve high-precision motion, a control strategy with superior servo capability to incorporate with the nature of magnetic actuators is synthesized. Each individual HMA consists of a permanent magnet to counterbalance the gravity of the intelligent disc and an electromagnet to control the posture of the intelligent disc. Since the electromagnetic system is highly nonlinear, a Feedback-Linearized Sliding Mode Control (FLSMC) is proposed to account for the system nonlinearities, uncertainties and unmodeled dynamics. Finally, intensive computer and experimental simulations are undertaken to validate the feasibility of the proposed SGRM and FLSMC.

2 OPERATION PRINCIPLE

The schematic diagram of the proposed Servo Gap-Retained Mechanism (SGRM) IS shown in Fig. 1. The SGRM mainly consists of an induction motor, a flywheel, an intelligent disc and four identical Hybrid Magnetic Actuators (HMAs). The intelligent disc can be adjusted to keep constant gap with

respect to the spinning eccentric flywheel which can tilt both about X - and Y -axes and whose center of mass can translate along X -, Y - and Z -axes. The flywheel, which is assumed as a rigid body, is connected to the induction motor by a flexible coupling. The spinning speed of the flywheel is governed by the induction motor. The intelligent disc, which is also a rigid body, is equipped beneath the flywheel with a nominal gap. The universal joint is employed as the pivot of the intelligent disc such that the intelligent disc can conduct 3-DOFs rotations, *i.e.*, yaw, pitch and spin. All the centroids of the induction motor, the flywheel, the intelligent disc and the universal joint are aligned vertically before the flywheel starts to spin. In addition, the flywheel is eccentric so that the tilting about X - and Y - axes occurs. Four identical HMAs are located ninety degrees apart under the intelligent disc to control its posture. Each individual HMA unit consists of a Permanent Magnet (PM) and an Electromagnet (EM) to cooperate to generate a resultant magnetic force to adjust the posture of the intelligent disc, as shown in Fig. 2. It is noted that the merits of employing HMAs, in which the same wire is wound around the same pair, not only reduce the number of power amplifiers but also considerably enhance the system stiffness of the SGRM. Significantly, adequate system stiffness can improve the bandwidth such that superior transient performance and servo capability of gap retaining by the intelligent disc can be, to some extent, ensured. On the other hand, four gap sensors, two for the flywheel and the others for intelligent disc, are used to acquire the real-time data of tilting of the flywheel and the intelligent disc.

The dynamics of the SGRM can be divided into two parts. One is the flywheel system, which consists of the flywheel itself and the flexible coupling. The other is the Intelligent Posture Tracking System (IPTS), which consists of the intelligent disc and the HMAs. The posture of the flywheel, in fact, is the target of tracking by the intelligent disc. Therefore, for the purpose of posture tracking, the dynamics of the flywheel system has to be modeled on the base of the displacements in X - and Y -axes.

The reference frames of the flywheel are shown in Fig. 3. The coordinate $\{X, Y, Z\}$ denotes the inertial reference frame and $\{A, B, C\}$ the frame attached on the flywheel. S is the centroid of the flywheel, P the center of mass of the flywheel, e the eccentricity and θ the argument of the eccentric mass. γ^f , β^f and ϕ are the yaw angle, pitch angle and spin angle of the flywheel about X -, Y - and Z -

axes respectively. Since the vertically translational stiffness of the flexible coupling is relatively high, the translational displacement of the flywheel in Z -axis direction is relatively insignificant and can be neglected. The superscript “ f ” is referred to the flywheel. m^f is the mass of the flywheel. I_R^f and I_P^f are the transverse mass moment of inertia and the polar mass moment of inertia of the flywheel respectively. $\Omega = \dot{\phi}$ is the rotational speed of the flywheel. $\xi^f = e \sin \theta$ and $\eta^f = e \cos \theta$ are the projections of the eccentricity onto A - and B -axes respectively. By Lagrange’s method, the equations of motion of the flywheel can be obtained as follows:

$$I_R^f \ddot{\beta}^f = I_P^f \Omega \dot{\gamma}^f \quad (1a)$$

$$I_R^f \dot{\gamma}^f = -I_P^f \Omega \dot{\beta}^f \quad (1b)$$

$$m^f \ddot{v}^f = m^f \Omega^2 \eta^f \sin \Omega t + m^f \Omega^2 \xi^f \cos \Omega t \quad (1c)$$

$$m^f \ddot{w}^f = m^f \Omega^2 \eta^f \cos \Omega t - m^f \Omega^2 \xi^f \sin \Omega t \quad (1d)$$

Because the dynamics of the flywheel system is directly influenced by the flexible coupling, the dynamics of the flexible coupling is analyzed by Timoshenko beam theory and modeled by Finite Element Method (FEM). A finite element of the flexible coupling is shown in Fig. 4. An element of the flexible coupling consists of two nodes. Each node has four DOFs. The translational displacements of an element of the flexible coupling can be described as $w(s, t)$ and $v(s, t)$ in X - and Y -axes directions respectively and the rotational displacements are $\gamma(s, t)$ and $\beta(s, t)$ respectively. The displacements of an element of the flexible coupling can be constructed as follows:

$$\begin{bmatrix} w(s, t) \\ v(s, t) \end{bmatrix} = \Psi(s) \mathbf{q}_e^T(t) \quad (2a)$$

$$\begin{bmatrix} \gamma(s, t) \\ \beta(s, t) \end{bmatrix} = \Phi(s) \mathbf{q}_e^T(t) \quad (2b)$$

where the superscript “ T ” denotes transpose operator. s is the axial position along an element, t the time instant and $\mathbf{q}_e = [q_1, q_2, \dots, q_8]$ the element displacement vector of the flexible coupling. Ψ and Φ are the mode shape functions.

Eventually, the equations of motion of the flywheel system with flexible coupling can be constructed by combining Eq. (1) with Eq. (2) as follows:

$$(\mathbf{M} + \mathbf{N}) \ddot{\mathbf{q}} + \Omega \mathbf{G} \dot{\mathbf{q}} + \mathbf{K} \mathbf{q} = \mathbf{h}_s \sin \Omega t + \mathbf{h}_c \cos \Omega t \quad (3)$$

where \mathbf{M} , \mathbf{N} , \mathbf{G} and \mathbf{K} are the translational mass

matrix, the rotational mass matrix, the gyroscopic matrix and the system stiffness matrix of the flywheel system respectively. \mathbf{h}_s and \mathbf{h}_c are the eccentric forces induced by eccentricity. Details of matrices \mathbf{M}^f , \mathbf{N}^f , \mathbf{G}^f , \mathbf{h}_s^f and \mathbf{h}_c^f are defined in the *Appendix*.

The intelligent disk has to follow the motion of the flywheel in the directions of pitch and yaw. To sum up, the equations of motion of the intelligent disc can be described as follows:

$$I_R^d \ddot{\gamma}^d + I_R^d (\dot{\beta}^d)^2 \sin \gamma^d \cos \gamma^d - I_P^d (\dot{\beta}^d)^2 \sin \gamma^d \cos \gamma^d = M_\gamma \quad (4a)$$

$$I_R^d \ddot{\beta}^d \cos^2 \gamma^d + I_P^d \ddot{\beta}^d \sin^2 \gamma^d - 2I_R^d \dot{\beta}^d \dot{\gamma}^d \sin \gamma^d \cos \gamma^d + 2I_P^d \dot{\beta}^d \dot{\gamma}^d \sin \gamma^d \cos \gamma^d = M_\beta \quad (4b)$$

where M_γ and M_β are the torques induced by the HMAs in the γ - and β -axes (i.e., yaw and pitch) respectively. The superscript “ d ” is referred to the intelligent disk.

The physical parameters of the flywheel system and the IPTS are listed in Tables 1 and 2 respectively. In order to reveal the nature of the flywheel dynamics, the open-loop of the gap-retained mechanism is examined at first. The time response and frequency response of the yaw angle of the flywheel are shown in Figs. 5 and 6 respectively. As shown in Fig. 6, the first natural frequency of the flywheel system, 13.73 Hz, is the fundamental frequency due to the flexible coupling, and the second, 16.79 Hz, is the first natural frequency of the rotational motion of the flywheel. It is evident that the first two frequencies of the flywheel system are very close to each other. Therefore, the amplitude of the time response, shown in Fig. 5, is slowly varying as time is running. The frequency of the time response is simply the average of those two frequencies. That is, it is the so-called *beat phenomenon* (Thomson, 1997) which is inherently embedded in the flywheel system.

It is evident from Eq. (3) that the HMA is a highly nonlinear system. Theoretically, the magnetic force of the HMA is proportional to the square of the applied current and inverse square of the air gap. In addition, an electromagnetic actuator is inherently an unstable system (Tsai, 2010). Therefore, a closed-loop control is absolutely necessary to stabilize the unstable system.

3 CONTROL STRATEGY

The proposed control strategy is based on feedback linearization theory (Matas, 2008) and synthesized via sliding mode approach (Shankar, 1999). The main concept of feedback linearization is to simplify the nonlinear system by means of feedback so that an approximate linear relation between the inputs and outputs of the closed-loop system can be constructed. Finally, a Sliding Mode Control (SMC) loop is synthesized to ensure the desired performances.

The dynamics of the IPTS can be rewritten as follows:

$$\dot{\mathbf{x}} = \boldsymbol{\chi}(\mathbf{x}(t)) + \boldsymbol{\kappa}(\mathbf{x}(t)) \mathbf{u} \quad (5a)$$

$$\mathbf{y} = \boldsymbol{\vartheta}(\mathbf{x}(t)) \quad (5b)$$

where

$$\mathbf{x} = [x_1 \quad x_2 \quad x_3 \quad x_4]^T = [\gamma^d \quad \dot{\gamma}^d \quad \beta^d \quad \dot{\beta}^d]^T \quad (6a)$$

$$\boldsymbol{\chi} = [\chi_1 \quad \chi_2 \quad \chi_3 \quad \chi_4]^T \quad (6b)$$

$$\boldsymbol{\kappa} = \begin{bmatrix} \frac{1}{I_R^d} & 0 \\ 0 & \frac{1}{I_R^d \cos^2 x_1 + I_P^d \sin^2 x_1} \end{bmatrix} \quad (6c)$$

$$\mathbf{u} = [M_\gamma \quad M_\beta]^T \quad (6d)$$

$$\mathbf{y} = [y_1 \quad y_2]^T \quad (6e)$$

$$\boldsymbol{\vartheta} = [x_1 \quad x_3]^T \quad (6f)$$

$$\chi_1 = x_2 \quad (6g)$$

$$\chi_2 = \frac{(I_P^d - I_R^d)}{I_R^d} x_4^2 \sin x_1 \cos x_1 \quad (6h)$$

$$\chi_3 = x_4 \quad (6i)$$

$$\chi_4 = \frac{1}{I_R^d \cos^2 x_1 + I_P^d \sin^2 x_1} \cdot [2(I_R^d - I_P^d) x_4 x_2 \sin x_1 \cos x_1] \quad (6j)$$

where x_1 and x_3 are the pitch and yaw of the intelligent disk respectively while x_2 and x_4 are the pitch rate and yaw rate respectively. \mathbf{x} denotes the state vector of the intelligent disk dynamics, $\boldsymbol{\chi}$ the nonlinear system dynamics, $\boldsymbol{\kappa}$ the input matrix, \mathbf{u} the system input vector, \mathbf{y} the measurement vector and $\boldsymbol{\vartheta}$ the output vector. By input-output linearization, the system output has to be differentiated, with respect to time, until it is explicitly related to the system input (Matas, 2008),

i.e.,

$$\mathbf{y}^{(\delta)} = \Lambda(\mathbf{x}) + \Gamma(\mathbf{x}) \mathbf{u} \quad (7)$$

where

$$\mathbf{y}^{(\delta)} = [\ddot{y}_1 \quad \ddot{y}_2]^T \quad (8a)$$

$$\Lambda(\mathbf{x}) = \begin{bmatrix} \frac{(I_P^d - I_R^d)}{I_R^d} x_4^2 \sin x_1 \cos x_1 \\ 1/(I_R^d \cos^2 x_1 + I_P^d \sin^2 x_1) \\ \bullet [2(I_R^d - I_P^d) x_4 x_2 \sin x_1 \cos x_1] \end{bmatrix} \quad (8b)$$

$$\Gamma(\mathbf{x}) = \begin{bmatrix} \frac{1}{I_R^d} & 0 \\ 0 & \frac{1}{I_R^d \cos^2 x_1 + I_P^d \sin^2 x_1} \end{bmatrix} \quad (8c)$$

δ is the order of the differential Eq. (6). Because the target of the SGRM is to adjust the yaw angle and pitch angle of the intelligent disc to track those of the flywheel, the sliding hyperplane can be defined as follows:

$$\Sigma(t) = [\Sigma_1 \quad \Sigma_3] \quad (9)$$

where

$$\Sigma_1 = \dot{e}_1 + \alpha_{11} e_1 + \alpha_{10} \int e_1 dt = 0 \quad (10a)$$

$$\Sigma_3 = \dot{e}_3 + \alpha_{31} e_3 + \alpha_{30} \int e_3 dt = 0 \quad (10b)$$

where $e_1 = x_1 - \gamma^f$ and $e_3 = x_3 - \beta^f$. The coefficients α_{11} , α_{10} , α_{31} and α_{30} are the design parameters and all positive. Based on the sliding hyperplane, the composite control can be constructed as follows:

$$\begin{bmatrix} M_\gamma \\ M_\beta \end{bmatrix} = \Gamma^{-1} \left(\begin{bmatrix} \ddot{\gamma}^d - \alpha_{11} \dot{e}_1 - \alpha_{10} e_1 \\ \ddot{\beta}^d - \alpha_{31} \dot{e}_3 - \alpha_{30} e_3 \end{bmatrix} - \begin{bmatrix} \Lambda_1 \\ \Lambda_3 \end{bmatrix} - \begin{bmatrix} \rho_1 \text{Sat}(\Sigma_1) \\ \rho_3 \text{Sat}(\Sigma_3) \end{bmatrix} \right) \quad (11)$$

where

$$\begin{bmatrix} \Lambda_1 \\ \Lambda_3 \end{bmatrix} = \begin{bmatrix} \frac{(I_P^d - I_R^d)}{I_R^d} x_4^2 \sin x_1 \cos x_1 \\ 1 \\ \bullet [2(I_R^d - I_P^d) x_4 x_2 \sin x_1 \cos x_1] \end{bmatrix} \quad (12)$$

ρ_1 and ρ_3 are the reaching factors and both positive. "Sat" is the saturation function.

It is noted that since the proposed control strategy is based on feedback linearization technique, the uncontrolled states of the system, which are referred to as the *internal dynamics* or *zero dynamics* consistent with the constraint $\mathbf{y}(t) = 0$, must be ensured to be bounded (Matas, 2008). If the eigenvalues of the linearization of internal dynamics lie in left half plane of the complex plane, the system is *locally exponentially*

minimum phase. That is, the internal dynamics is bounded. In other words, the stability of controlled states, i.e., x_1 and x_3 , can be ensured by Eq. (11) and Eq. (12). Once the eigenvalues of the linearization of internal dynamics all lie in left half plane of the complex plane, the stability of entire system can be ensured.

4 EXPERIMENTAL RESULTS

The test rig of the SGRM is shown in Fig. 7. The experiments are undertaken under the interface module *DS1104* by *dSPACE* and the environment by *Matlab/Simulink*. The proposed FLSMC is implemented using TMS320F240 DSP with 10 kHz sampling frequency. Two gap sensors, Model KD-2300 by *KAMAN Instrumentation Corporation*, are employed to acquire the angular displacements of the flywheel at the top side about X- and Y-axes. The other two are used to measure the angular displacements of intelligent disc below the intelligent disc about X- and Y-axes. Two sets of power amplifiers are also employed to implement the control commands for the intelligent disc to retain constant gap with respect to the eccentric flywheel. The commands at digital controller are processed by D/A (Digital to Analog) converter at first. Since the power amplifiers are of the transconductance type, it becomes simpler to just control the applied current at magnetic actuators directly. The power amplifier, Chip PA12A by *APEX*, has wide bandwidth and superior linearity and is employed as the voltage-current converter in this work. The output current of PA12A is allowed up to 15 A, which is large enough to energize the electromagnets at HMAs.

Under FLSMC law, the time response of tilt displacement (i.e., yaw angle) of the proposed SGRM is shown in Fig. 8. The rotational speed of the induction motor is preset at 2400 RPM and the wobbled frequency of the flywheel is about 80 Hz. After 0.07 sec, the tracking error, shown in Fig. 9, is reduced to below 5% of the amplitude of the tilt displacement. It is observed that the proposed SGRM possesses superior transient response and servo capability upon tracking of the eccentric flywheel. In addition, the applied current at HMAs is shown in Fig. 10. Because the HMA is designed to include PM (Permanent Magnet), the bias current for the HMA to counterbalance the gravity of the intelligent disc is almost negligible. Therefore, the amplitude of applied current for EMs (Electromagnets) is only about 0.6 A. The

experimental setup and result for the flywheel discharge (i.e., from kinetic energy to electric energy) are shown in Fig. 11 and Fig. 12 respectively.

5 CONCLUSIONS

An innovative intelligent disc, with magnetic actuators, to retain a constant gap with respect to a spinning eccentric flywheel which spins, tilts and wobbles. The magnetic actuators are designed to include both EMs (Electromagnets) and PMs (Permanent Magnets) so that most of the gravity of the intelligent disc is counterbalanced by PMs. A Feedback-Linearized Sliding Mode Control (FLSMC) is synthesized to account for system nonlinearities or unmodeled dynamics. The entire mechanism, excluding the flywheel, is named as a SGRM (Servo Gap-Retained Mechanism). The SGRM is verified both by computer simulations and experiments. Not only is the system stiffness greatly enhanced, but also the number of power amplifiers and energy consumption are both reduced. It is shown that the gap between the flywheel and the intelligent disc can be retained. The corresponding settling time is less than 0.07 sec and the worse tracking error is below 5%. The required control current at the EMs is always less than 0.75 A. From the experimental result, even though the upper bound of system parameters uncertainty is up to 15%, FLSMC is capable to stabilize the gap-retain dynamics and sustain excellent performance.

ACKNOWLEDGEMENTS

This research was partially supported by *National Science Council* (Taiwan) with 3-year Grant 98-2221-E-006-184-MY3. The authors would like to express their appreciation.

REFERENCES

- Li, Y., Xing, J., Han, S., Lu, Y., 2009. Principle and simulation analysis of a novel structure non-contact electromagnetic clutch, *The 12th Int. Conf. Electr. Mach. Syst.*
- Matas, J., Castilla, M., Guerrero, J. M. de Vicuña, L. G. Miret, J., 2008. Feedback linearization of direct-drive synchronous wind-turbines via a sliding mode approach, *IEEE Trans. Power Electron.* 23(3) pp.1093-1103.

- Shankar, S., 1999. *Nonlinear Systems: Analysis, Stability, and Control*, Springer, New York.
- Thomson, W. T., Dahleh, M. D., 1997. *Theory of vibration with applications*, Prentice Hall, 1997.
- Tsai, N.-C., Chiang, C.-W., 2010. Spindle position regulation for wind power generators, *Mech. Syst. Signal Process.* 24(3) pp. 873-889.

APPENDIX

Table 1: Parameters of Gap-Retained Mechanism.

Parameter	Notation	Numerical Value	Unit
Mass of Flywheel	m_d	0.9861	kg
Eccentric Angle	θ	0.7854	rad
Eccentric Distance	e	12e-3	m
Polar Mass Moment of Inertia (Flywheel)	${}_p I_d$	0.0111	kgm ²
Transverse Mass Moment of Inertia (Flywheel)	${}_R I_d$	0.0080	kgm ²
Cross-Section Area of Coupling	A	3.2673e-4	m ²
Length of Coupling	L	50e-3	m
Density of Coupling	ρ	1280	Kg/m ³
Young's Modulus	E	1e6	N/m ²
Shear Modulus	G_s	1250e3	N/m ²
Shear Factor	K_s	0.9	Dimensionless
Polar Mass Moment of Inertia (Coupling)	${}_p \hat{I}_e$	1.4156e-4	kgm ²
Transverse Mass Moment of Inertia (Coupling)	${}_R \hat{I}_e$	8.1660e-5	kgm ²
Area Moment of Inertia (Coupling)	${}_m I_e$	1.1060e-7	m ⁴
Rotational Speed of Motor	Ω	1000	rpm

Table 2: Parameters of IPTS.

Parameters	Notations	Numerical Values	Unit
Transverse Mass Moment of Inertia of Intelligent Disc	I_R^d	0.0155	Kg-m ²
Polar Mass Moment of Inertia of Intelligent Disc	I_P^d	0.0078	Kg-m ²
Lengths from Pivot of Intelligent Disc to HMAs	ℓ_γ, ℓ_β	0.092	m
Area of Air Gap	A_G	8×10^{-4}	m ²
Area of PM	A_P	4.5×10^{-4}	m ²
Air Gap	G_A	3×10^{-3}	m
Width of PM	W	0.02	m
Flux Density of PM	B_P	1.3	Tesla
Turns of Wound Coil	N_c	300	—
Correction Factor	λ	0.71	—

The matrices \mathbf{M}^f , \mathbf{N}^f , \mathbf{G}^f , \mathbf{h}_s^f and \mathbf{h}_c^f are defined as follows:

$$\mathbf{M}^f = \begin{bmatrix} m^f & 0 & 0 & 0 \\ 0 & m^f & 0 & 0 \\ 0 & 0 & 0 & 0 \\ 0 & 0 & 0 & 0 \end{bmatrix} \quad (\text{A1})$$

$$\mathbf{N}^f = \begin{bmatrix} 0 & 0 & 0 & 0 \\ 0 & 0 & 0 & 0 \\ 0 & 0 & I_R^f & 0 \\ 0 & 0 & 0 & I_P^f \end{bmatrix} \quad (\text{A2})$$

$$\mathbf{G}^f = \begin{bmatrix} 0 & 0 & 0 & 0 \\ 0 & 0 & 0 & 0 \\ 0 & 0 & 0 & I_R^f \\ 0 & 0 & -I_P^f & 0 \end{bmatrix} \quad (\text{A3})$$

$$\mathbf{h}_s^f = m^f \Omega^2 \begin{bmatrix} -\xi^f & \eta^f & 0 & 0 \end{bmatrix}^T \quad (\text{A4})$$

$$\mathbf{h}_c^f = m^f \Omega^2 \begin{bmatrix} \eta^f & \xi^f & 0 & 0 \end{bmatrix}^T \quad (\text{A5})$$

The detail descriptions of the mode shape functions are expressed as follows:

$$\Psi(s) = \begin{bmatrix} \psi_1 & 0 & 0 & \psi_2 & \psi_3 & 0 & 0 & \psi_4 \\ 0 & \psi_1 & \psi_2 & 0 & 0 & \psi_3 & \psi_4 & 0 \end{bmatrix} \quad (\text{A6})$$

$$\Phi(s) = \begin{bmatrix} 0 & \phi_1 & \phi_2 & 0 & 0 & \phi_3 & \phi_4 & 0 \\ \phi_1 & 0 & 0 & \phi_2 & \phi_3 & 0 & 0 & \phi_4 \end{bmatrix} \quad (\text{A7})$$

where

$$\psi_1 = \frac{1}{1+\Theta} [2a^3 - 3a^2 + 1 + \Theta(1-a)] \quad (\text{A8})$$

$$\psi_2 = \frac{L}{1+\Theta} [a^3 - 2a^2 + a + \Theta(-\frac{a^2}{2} + \frac{a}{2})] \quad (\text{A9})$$

$$\psi_3 = \frac{1}{1+\Theta} [-2a^3 + 3a^2 + \Theta a] \quad (\text{A10})$$

$$\psi_4 = \frac{L}{1+\Theta} [a^3 - a^2 + \Theta(\frac{a^2}{2} - \frac{a}{2})] \quad (\text{A11})$$

$$\phi_1 = \frac{1}{1+\Theta} \left[\frac{1}{L} (6a^2 - 6a) \right] \quad (\text{A12})$$

$$\phi_2 = \frac{1}{1+\Theta} [3a^2 - 4a + 1 + \Theta(-a + 1)] \quad (\text{A13})$$

$$\phi_3 = \frac{1}{1+\Theta} \left[\frac{1}{L} (-6a^2 + 6a) \right] \quad (\text{A14})$$

$$\phi_4 = \frac{1}{1+\Theta} (3a^2 - 2a + \Theta a) \quad (\text{A15})$$

$$\Theta = \frac{12EI_e^c}{K_s G_s AL^2} \quad (\text{A16})$$

$$a = \frac{s}{L} \quad (\text{A17})$$

It is noted that the shear effect has been taken into consideration for mode shape functions.

The matrices \mathbf{M} , \mathbf{N} , \mathbf{G} , \mathbf{K} , \mathbf{h}_s and \mathbf{h}_c are defined as follows:

$$\mathbf{M} = \sum \mathbf{M}_e + \mathbf{M}^f \quad (\text{A18})$$

$$\mathbf{N} = \sum \mathbf{N}_e + \mathbf{N}^f \quad (\text{A19})$$

$$\mathbf{G} = \sum \mathbf{G}_e + \mathbf{G}^f \quad (\text{A20})$$

$$\mathbf{K} = \sum \mathbf{K}_e \quad (\text{A21})$$

$$\mathbf{h}_s = \sum \mathbf{h}_{se} + \mathbf{h}_s^f \quad (\text{A22})$$

$$\mathbf{h}_c = \sum \mathbf{h}_{ce} + \mathbf{h}_c^f \quad (\text{A23})$$

$$\mathbf{M}_e = \rho A \int_0^L (\psi_w^T \psi_w + \psi_v^T \psi_v) ds \quad (\text{A24})$$

$$\mathbf{N}_e = \hat{I}_R \int_0^L (\phi_\Gamma^T \phi_\Gamma + \phi_\beta^T \phi_\beta) ds \quad (\text{A25})$$

$$\mathbf{G}_e = \hat{I}_P \int_0^L (\phi_\Gamma^T \phi_\beta - \phi_\beta^T \phi_\Gamma) ds \quad (\text{A26})$$

$$\mathbf{K}_e = E \hat{I} \int_0^L (\phi'_\beta \phi'_\beta + \phi'_\Gamma \phi'_\Gamma) ds \quad (\text{A27})$$

$$+ K_s G_s A \int_0^L \{ (\psi_v^T \psi'_v - \psi_v^T \phi_\Gamma) - \phi_\Gamma^T \psi'_v + \phi_\Gamma^T \phi + (\psi_w^T \psi'_w - \psi_w^T \phi_\beta) - \phi_\beta^T \psi'_w + \phi_\beta^T \phi \} ds$$

$$\mathbf{h}_{se} = \rho A \Omega^2 \int_0^L \Psi^T \begin{bmatrix} -\xi(s) \\ \eta(s) \end{bmatrix} ds \quad (\text{A28})$$

$$\mathbf{h}_{ce} = \rho A \Omega^2 \int_0^L \Psi^T \begin{bmatrix} \eta(s) \\ \xi(s) \end{bmatrix} ds \quad (\text{A29})$$

where

$$\eta(s) = \eta_0 (1 - \frac{s}{L}) + \eta_L (\frac{s}{L}) \quad (\text{A30})$$

$$\xi(s) = \xi_0 (1 - \frac{s}{L}) + \xi_L (\frac{s}{L}) \quad (\text{A31})$$

(η_0, ξ_0) and (η_L, ξ_L) indicate that the eccentricity at $s=0$ and $s=L$ respectively.

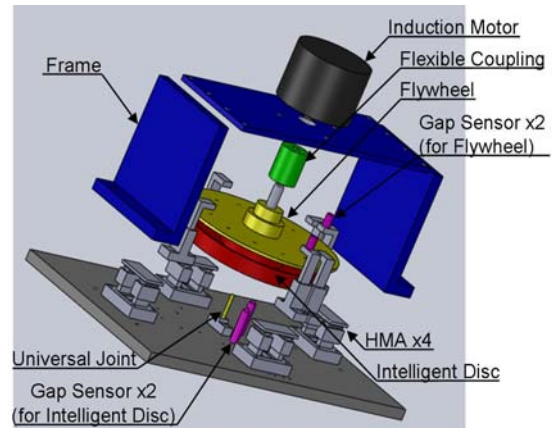


Figure 1: Diagram of Servo Gap-Retained Mechanism.

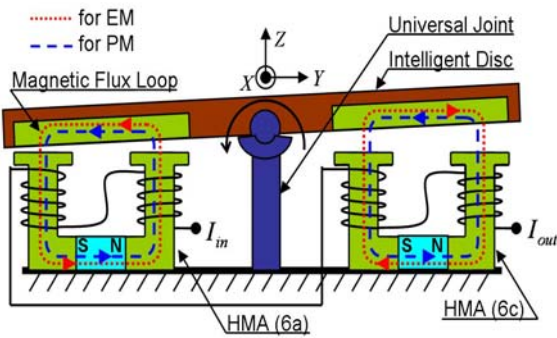


Figure 2: Magnetic Flux Path and Mechanism of HMAs.

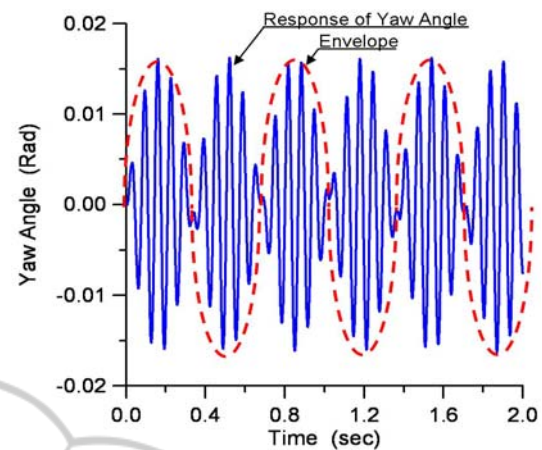
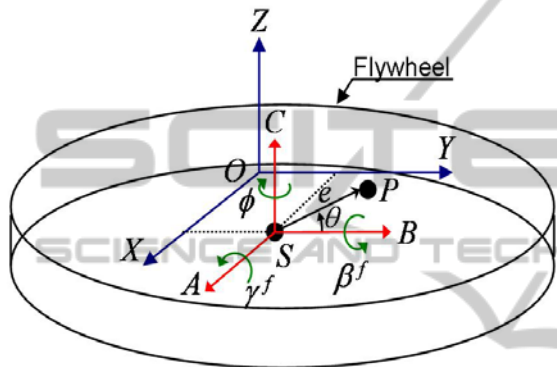


Figure 5: Time Response of Yaw of Flywheel.



e : Eccentricity
 θ : Argument of Eccentric Mass

Figure 3: Reference Frames of Flywheel.

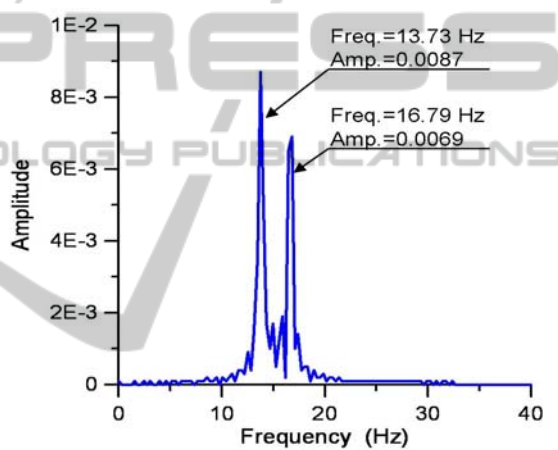


Figure 6: Frequency Response of Yaw of Flywheel.

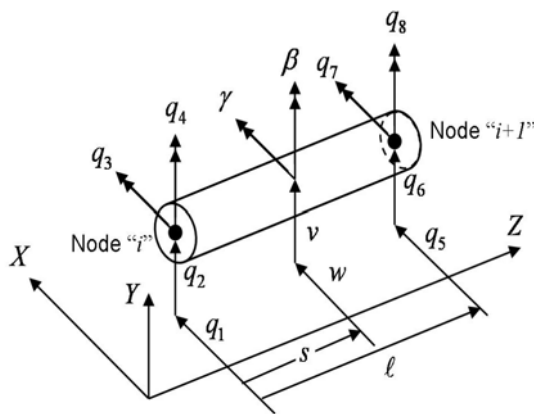


Figure 4: Finite Element of Flexible Coupling.

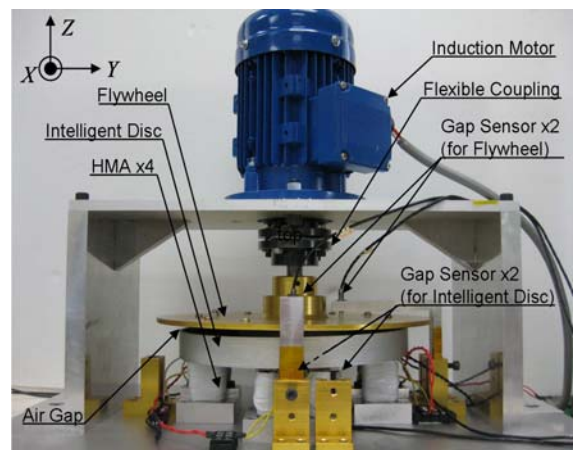


Figure 7: Test Rig of SGRM.

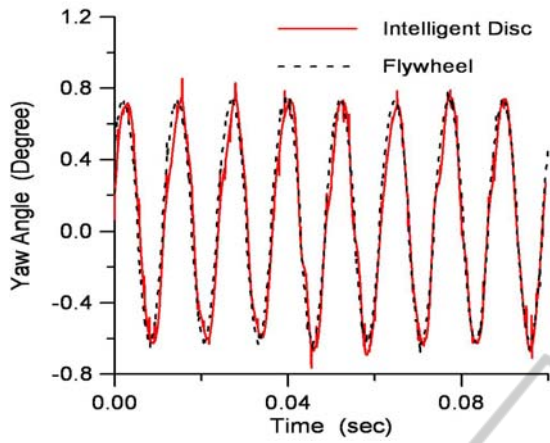


Figure 8: Time Response of Yaw of SGRM under FLSMC Law by Experiment.

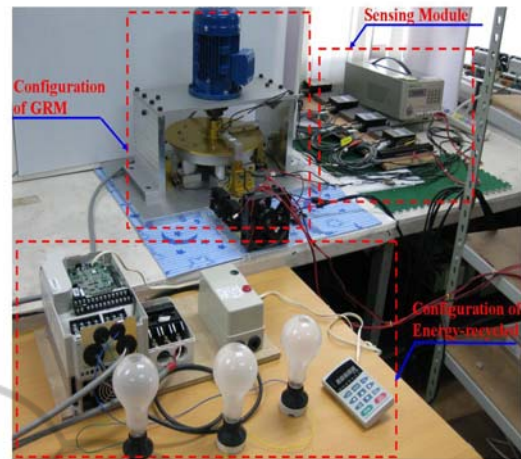


Figure 11: Experimental Setup for Flywheel Cell Discharge.

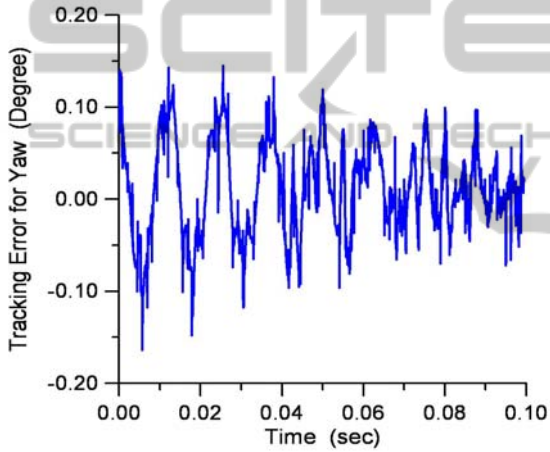


Figure 9: Tracking Error of Yaw of SGRM under FLSMC Law by Experiment.

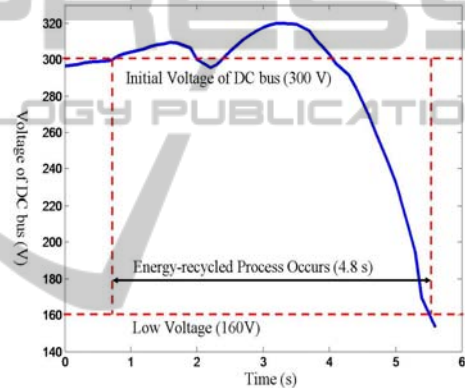


Figure 12: Discharge Curve for Flywheel Cell by Experiment.

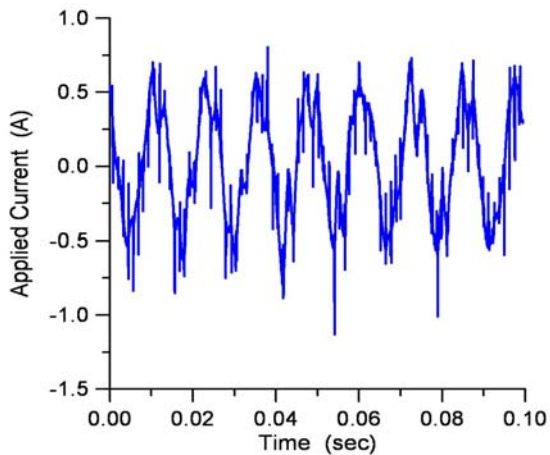


Figure 10: Applied Current for Yaw Tracking by Experiment.